

SparkJet Efficiency

Mona Golbabaie-Asl^{*} and Doyle Knight[†] and Kellie Anderson[‡]

Rutgers - The State University of New Jersey, New Brunswick, New Jersey 08903, USA

Stephen Wilkinson[§]

NASA Langley Research Center, Hampton, Virginia 23681, USA

A novel method for determining the thermal efficiency of the SparkJet is proposed. A SparkJet is attached to the end of a pendulum. The motion of the pendulum subsequent to a single spark discharge is measured using a laser displacement sensor. The measured displacement *vs* time is compared with the predictions of a theoretical perfect gas model to estimate the fraction of the spark discharge energy which results in heating the gas (*i.e.*, increasing the translational-rotational temperature). The results from multiple runs for different capacitances of $c = 3, 5, 10, 20$, and $40\mu\text{F}$ show that the thermal efficiency decreases with higher capacitive discharges.

I. Introduction

ELECTROMAGNETIC Local Flow Control (ELFC) is the application of pulsed electromagnetic fields to modify flow structure for improving design performance or alleviating adverse flow conditions. A wide variety of ELFC devices have been developed including, for example, Dielectric Barrier Discharge (DBD), laser and/or microwave discharge, electron beam, and surface DC/AC discharge.¹⁻⁴

The Johns Hopkins University Applied Physics Laboratory has developed a unique ELFC device denoted the SparkJetTM for flow and flight control.⁵⁻¹¹ The basic concept is illustrated in Fig. 1. A spark is discharged within a typical volume of several cm^3 (Stage 1). The high pressure gas discharges through a converging nozzle thereby generating an impulse (Stage 2). Provided there is a mechanism for recharging the gas in the cavity (Stage 3), the sequence can be repeated. Research has also been conducted at the University of Texas at Austin,¹² ONERA¹³ and Rutgers University.¹⁴

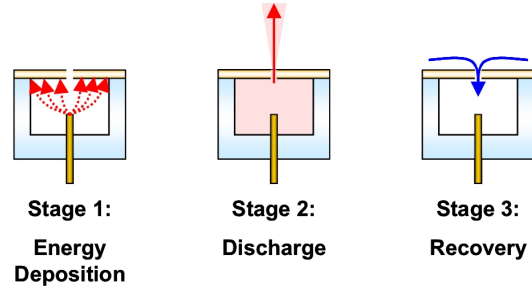


Figure 1. SparkJet⁷

The objective of the paper is the determination of the thermal energy efficiency of a *particular* design of a SparkJet. The thermal energy efficiency is the fraction of the electrical energy which results in effective heating of the gas in the cavity. The spark discharge generates a plasma with excited electronic, rotational, and vibrational states. A portion of the energy dissipated across the spark gap is channeled into heating of the gas (*i.e.*, increasing the translational-rotational temperature) which leads to a high pressure and subsequent jet exiting through the converging nozzle. Various estimates of the thermal energy efficiency have been published.^{10,11} In this paper, a novel method for determining energy efficiency is proposed based upon comparison of predictions of a theoretical model and experimental measurements.

^{*}Ph.D. Candidate, Department of Mechanical and Aerospace Engineering, AIAA Member.

[†]Professor, Department of Mechanical and Aerospace Engineering, AIAA Member.

[‡]Post-Doctoral Researcher, Department of Chemical and Bio-Chemical Engineering.

[§]Senior Scientist, Flow Physics and Control Branch, AIAA Member.

II. Experiment

II.A. Pendulum

A prototype pendulum apparatus and SparkJet actuator was constructed in order to measure the impulse response of a single capacitive discharge. The pendulum apparatus is shown schematically in Fig. 2. It consisted of a wooden pendulum, a low friction pivot assembly, a low torque electrical coupling, and a SparkJet actuator. The pendulum and pivot assembly was mounted in a rigid wooden stand shielded from room air drafts by transparent plastic (Plexiglass) panels. A photograph of the completed assembly with a close-up of the actuator is shown in Fig. 3(a).

The pendulum was a 12.7 mm diameter wooden (Maple) dowel mounted to a pivot block assembly on one end and to the SparkJet actuator on the opposite end. The pivot assembly consisted of a rectangular block of UHMW polyethylene ($19 \times 28 \times 63$ mm) with two sharp carbide scriber pins (from Moody Tools Model 51-1520) resting on hard glass surfaces. A photograph of the pivot assembly is shown in Fig. 3(b). Due to the very small angular displacement, typically less than 0.01 degree, friction was relied upon to maintain the pins in a fixed position on the glass surface. Small translations of the pins on the glass surface due to the SparkJet impulse that may have occurred during testing were corrected for the theoretical analysis. Indentations in the glass could have been used to guarantee no movement of the pins but they were not used out of concern of increasing bearing torque. The mass moment of inertia for a compound pendulum can be computed from the total rotating mass m , the distance from the pivot axis to the center of the mass L_{cg} , and the pendulum period T , *i.e.*, $I = mgL_{cg}(\frac{T}{2\pi})^2$ kg·m².

A low torque electrical coupling was fabricated by suspending low stiffness conductors between two screw-terminal blocks, one attached to the stationary wooden support stand and the other to the rotating pivot block (See Fig. 2 and 3(b)). For the high current, capacitive discharge conductors, 2.4 mm diameter brass ball chain was used. The chain will not support a bending moment but is a good electrical conductor. A drawback of the chain was that arcing was occasionally noticed between the balls suggesting an irregular voltage drop. Since the actuator spark gap voltage was recorded, minor chain arcing and irregularities in the chain voltage drop was not judged to be a serious issue. For spark gap voltage monitoring where connecting wire voltage drop was not an issue (due to the high impedance oscilloscope probe and very low current), very small diameter copper wire (38 AWG, 0.1 mm dia.) with negligible stiffness was used.

The supply wires for the trigger, capacitor discharge and ground return between the power supply and trigger source and pivot block assembly were, 21 AWG (~ 0.7 mm dia.) copper wire. The current carrying wires between the pivot block and actuator were 18 AWG (~ 1 mm dia.), wire attached parallel to the pendulum shaft. The spark gap voltage monitor wires were 25 AWG (~ 0.46 mm dia.) installed parallel to the current carrying conductors. All wires were unshielded, stranded, and insulated copper and were secured to the pendulum shaft with bands of heat shrink tubing.

II.B. SparkJet Actuator

A capacitive-discharge, ionization-triggered, tri-electrode SparkJet actuator was fabricated following the design described.¹⁵ Referring to the schematic in Fig. 4, an unregulated, DC power supply (Acopian model U500Y20) was connected through resistor R_1 to capacitor C between nodes 1 and 4. The capacitor was in parallel with the spark gap between nodes 2 and 3. The value of R_1 was fixed at 5 KOhm to limit charging current and isolate the spark gap from the power supply. The capacitor C was replaceable and had values of 3, 5, 10, 20, and 40 μ F (Genteq Model GEM-III rated at 1000 VDC peak/440 VAC). Diode D was used to prevent high back emf transients due to the collapsing magnetic field in loop 1 – 2 – 3 – 4 from generating a secondary discharge.

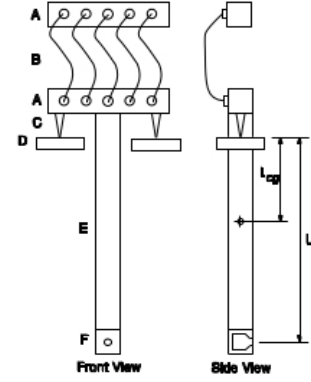
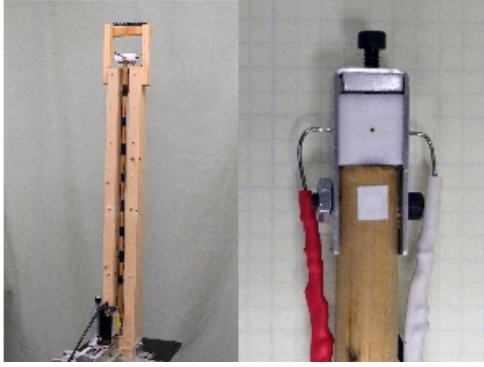
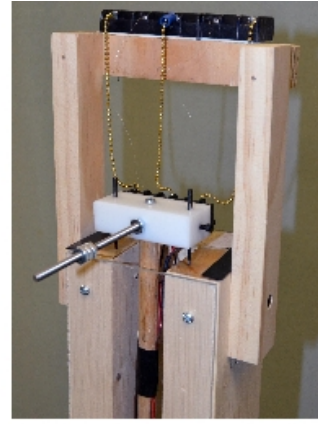


Figure 2. Schematic view of pendulum apparatus (not to scale). A. screw terminal block, B. connecting chains and wires, C. sharp carbide pins, D. stationary glass bearing surface, E. wood dowel, F. SparkJet actuator. $L = 797.8$ mm, L_{cg} (center of gravity) = 291.4 mm, Total rotating mass (exclusive of connecting chains and wires) = 190.43 gram



(a) Photograph of pendulum apparatus with close-up of SparkJet actuator. The trigger electrode enters from the rear of the Teflon block. The gap voltage monitoring leads are silver soldered to the electrodes beneath the red and white insulation.



(b) Photograph of pivot assembly with low torque electrical chain and wire connectors. The outrigger screw post is used to adjust the vertical angle of the pendulum shaft due to the asymmetry of the pivot block with the attached screw terminal strip.

Figure 3. Photograph of a) pendulum, and b) pivot assembly and electrical coupling

An ionization trigger was used to discharge the capacitor by introducing an approximately 1 microsecond pulse, V_p , into step up transformer T to create a 25 kV pulse between nodes 5 and 3. The pulse was provided by a low cost, commercial trigger source (Information Unlimited, Model Ignitor10). Resistor R_2 helps to isolate the transformer from the spark gap while still allowing the ionization pulse to function. The circuit will function without R_2 but the influence of the transformer will be seen in the loop voltage measurements, particularly V_{12} and V_{34} complicating interpretation of the data.

Intensified CCD images of the trigger and discharge sparks are shown in Fig. 5(a) for a bench top (non-enclosed electrodes) setup of three electrodes in a equi-angle, 120 degree star arrangement. The electrode arrangement for the current actuator experiment (described below) was orthogonal rather than equi-angular but the dimensions are similar and discharge is assumed to behave similarly. The notation in Fig. 5(a) corresponds to the schematic in Fig. 4. The electrodes are 0.81 mm diameter Nichrome wire. The left frame shows the 25 kV trigger spark alone. The right hand frame shows the capacitive discharge for $C = 10\mu\text{F}$. The images are registered, 50% opaque overlays of separately acquired discharge and electrode images. As shown, the high voltage trigger pulse creates an ionization channel between nodes 5 and 3 that subsequently allows the capacitor to discharge along path 1 – 5 – 3.

Construction of the actuator is shown in Fig. 5(b). It consisted of a rectangular block of polytetrafluoroethylene (Teflon) with a cylindrical cavity, orifice, electrodes and a nylon set-screw end closure. The internal cavity volume was 234.2 mm^3 inclusive of the discharge orifice neck and accounting for the displacement volume of the three electrodes. The electrodes were 0.81 mm diameter nickel-chromium resistance wire (Nichrome). The electrodes penetrated the Teflon wall via an interference fit and were additionally bonded with cyanoacrylate glue to prevent movement. While the electrodes had initially flat, square ends, under use the sharp edges corroded slightly due to the electrical discharges forming smooth, rounded edges. The main capacitive discharge electrodes (nodes 1 and 4 in Fig. 4) were oriented directly opposed to each other with a spacing of approximately 0.8 mm. The trigger electrode (node 5) was positioned midway between the discharge pair and oriented at 90 degrees. The closest distance between electrodes 5 and 3 was approximately 0.5 mm. These were somewhat arbitrary offsets with the only requirement being that the trigger and discharge operate reliably. A small amount of electrode recession likely occurred over the duration of the experiment. The actuator was not designed for accurate measurement and maintenance of the spark gap

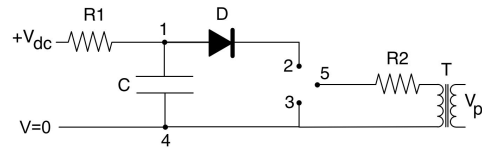
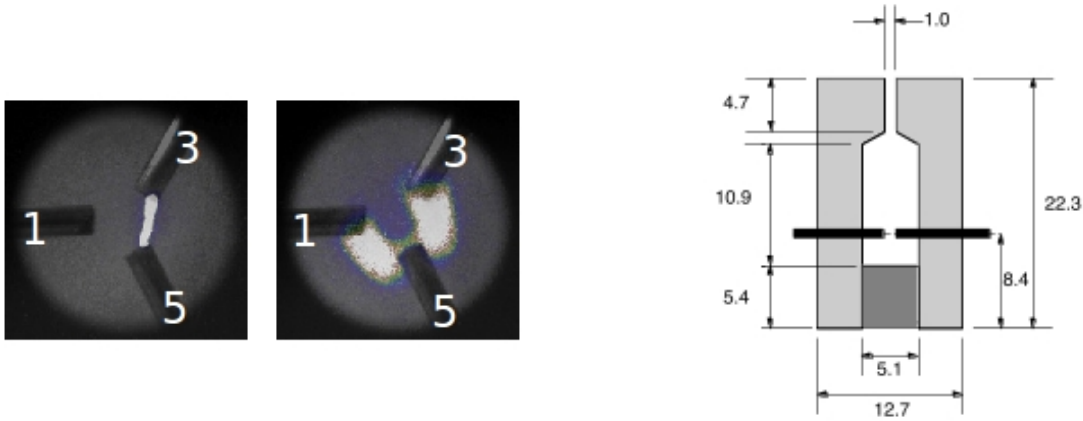


Figure 4. SparkJet electrical circuit schematic. $V_{dc} = 550$ volt unregulated, V_p trigger pulse from pulse generator, T pulse step up transformer, $R_1 = 5\text{ k}\Omega$, $R_2 = 1\text{ k}\Omega$, D diode (IN4007-30), C capacitor (3, 5, 10, 20, 40 μF)



(a) Instantaneous images of the tri-electrode SparkJet actuator. Image obtained with a Cooke DiCam Pro ICCD camera with S20Q photocathode and p_{43} output phosphor. 10 nanosecond exposure after 2700 nanosecond trigger delay. (b) Dimensioned cross-sectional diagram of SparkJet. All dimensions millimeter.

Figure 5. SparkJet: a) photograph and b) diagram

width. Increasing electrode separation requires greater power to produce a spark. Since both the gap voltage and current was measured, however, the effect of electrode recession on consumed power was accounted for.

II.C. Diagnostics

The maximum expected displacement of the pendulum was only a few tens of micrometers; therefore, accurate measurement of the displacement time history was a primary concern. A laser-based optical displacement sensor, Microepsilon optoNCDT model ILD-2200, was selected based on its range (2 mm), resolution (0.03 nm), stand-off distance (24 mm) and frequency response (20 kHz at -3 dB). The sensor has both analog and digital signal outputs. The analog output was used in this study.

Data was acquired on a digital oscilloscope, Agilent Model MSO7034A, rated at 8-bit resolution, ± 40 volt vertical dynamic range and 350 MHz bandwidth. The oscilloscope's "high resolution mode" was used to record the voltage and current signals. The high resolution mode effectively low pass filters the signals to remove noise and also is claimed to increase vertical resolution. The cutoff frequency is not specified in the user manual but is sufficiently high such that no difference in the current-voltage phase relationship was observed compared to the oscilloscope's normal resolution mode.

In order to determine the input energy required to the main discharge spark, both the instantaneous voltage across the gap and instantaneous loop current must be measured. Since the instantaneous current can be very high (on the order of 1000 amp), a large voltage drop is expected across both the supply and return legs of the wiring. As will be shown for this particular implementation, roughly two-thirds of the capacitor voltage is dropped across the supply wiring. For this reason, a separate pair of voltage monitoring leads was attached directly to the actuator electrodes close to the spark gap. Since the oscilloscope probe is high impedance (> 1 MOhm), negligible current flows in the monitor wires and the actual gap voltage can be accurately measured. The voltage-time waveforms were measured with an Agilent Model N2790A active differential probe rated at 1400 volt and 100 MHz. The differential probe avoided possible measurement errors by removing the ground side of the building AC power system from the measurement circuit. Initial measurements conducted with a single-ended, high voltage probe (Tektronix Model P6015A) delivered confusingly different waveforms and voltage levels depending on where ground wires were connected. This problem was completely avoided with the active differential probe. The active probe has two range settings, 50X and 500X. The 500X setting was used in these experiments.

Electrical current was measured with a Pearson Model 110 wideband current transformer rated at 0.1 amp/volt sensitivity, 5000 peak amps, 0.5 amp-second current-time product (a measure of core saturation) and a usable rise time of 20 nanoseconds. In the current experiment, maximum current-time product

was less than 0.02 amp-sec. The large amplitude current pulses caused the current transformer output to exceed the dynamic range of the oscilloscope. A 10X voltage divider probe, Agilent Model 10073C, was therefore used to record the current transformer output.

Since the trigger pulse has an amplitude of 25 kV, it could not be recorded with the differential oscilloscope probe that is limited to 1.4 kV. The trigger pulse was recorded and described by Reedy *et al.*¹⁵ showing that the trigger gap (node 5 – 3) rises until the breakdown voltage for the gap is reached followed by a rapid drop in gap voltage as the air ionizes. The high voltage trigger pulse width is typically less than 1 microsecond.

When the SparkJet was operated at even a low discharge frequency of a few Hertz, the digital laser displacement sensor and/or controlling PC would invariably lockup after a few seconds of operation due to the intense electromagnetic interference noise from capacitive discharge. When operated in single pulse mode, however, the subject of this investigation, such lockup occurred only rarely. Use of shielded cables, ferrite cores, and large separation distance between the actuator and recording equipment can reduce interference effects but none was required in this experiment.

Due to the undamped design of the pendulum and the light weight housing in which it was mounted, the pendulum was very sensitive to any structural vibrations in the laboratory. Even after several hours of isolation in an unoccupied lab after normal working hours, the pendulum never completely came to rest. To the contrary, the pendulum undergoes a continuous, random low level amplitude modulation that may be related to low level, background seismic activity. Vibration problems are typically treated with either high mass damping or some type of air flotation/damping or elastic resilient isolation mounts. For the purpose of estimating the impulse due to the SparkJet, however, an absolutely motionless initial condition is not required as long as the initial amplitude and phase is recorded at the moment of actuation. Since the period of the pendulum is low (~ 1.5 seconds), triggering at various phases angles was done manually by displaying the pendulum displacement signal on the oscilloscope in time "roll" mode, analogous to a paper strip chart recorder. When the displacement signal reached the desired phase quadrant, the spark was manually triggered. Finer phase selection using the manual method was not possible but after repeated trials, a useful range of phase angles was obtained.

III. Theoretical Model

III.A. Model Description

The SparkJet is attached to the end of a pendulum. The spark discharge within the cavity creates an air jet which generates a force and moves the pendulum. The geometry of the pendulum is shown in Fig. 6. Without the influence of the SparkJet, the pendulum moves with a small amplitude as a result of ambient noise which perturbs the pendulum (see Section II.C). The geometry of the cavity is shown in Figure 7. The cavity is initially at ambient pressure p_∞ and ambient temperature T_∞ . The energy deposited to the cavity, Q , is assumed to increase the temperature to T_{t_o} and pressure to p_{t_o} at a constant density ($\rho_{t_o} = \rho_\infty$) instantaneously at time t_0 .

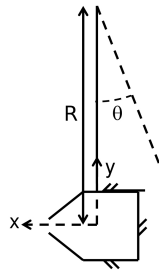


Figure 6. Dimensions of Pendulum

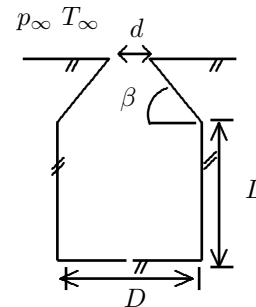


Figure 7. Cavity Geometry

An inviscid perfect gas model is assumed for the air flow to avoid elaborate computations required to account for thermochemical reactions. However, such an ideal model cannot represent the fraction of the deposited energy which results in the translational-rotational temperature increase in gas. Therefore, the initial total temperature of the gas in the cavity is

$$T_{t_o} = T_\infty + \frac{\eta Q}{\rho_\infty V c_v} \quad (1)$$

where ηQ is the effective heat added to the gas (*i.e.*, resulting in the increase in the translational-rotational temperature of the gas), ρ_∞ is the initial density of the gas in the cavity, V is the cavity volume and c_v is the specific heat at constant volume. The quantity η is denoted the *thermal efficiency* of the SparkJet. The thermal efficiency in percent is $100 \times \eta$. The above expression may be rewritten as

$$T_{t_o} = T_\infty [1 + (\gamma - 1)\epsilon] \quad (2)$$

where

$$\epsilon = \frac{\eta Q}{p_\infty V} \quad (3)$$

For a physical interpretation of ϵ , see Anderson and Knight.¹⁶

III.B. Governing Equations

Assuming that the pendulum motion is planar, the equation of motion for the pendulum is given by Newton's second law for rotating bodies

$$I \frac{d^2 \theta}{dt^2} + \int_0^R (gr \sin \theta) dm_p + m_s(t) g \sin \theta R = RF(t) \quad (4)$$

where m_p is the mass of the pendulum (assuming a uniform density and constant cross section), $m_s(t)$ is the mass of the SparkJet, R is the distance from the pendulum pivot point to the cavity center, $F(t)$ is the force from the cavity exhaust, and I is the moment of inertia of the pendulum plus cavity system.

$$I = \int_0^R r^2 dm_p + m_s(t) R^2 \quad (5)$$

assuming the dimension of the SparkJet is small compared to R . The mass of the gas inside the SparkJet is negligible compared to the mass of the SparkJet, and therefore $m_s(t)$ is assumed constant. Assuming $\theta \ll 1$ radian,

$$\frac{d^2 \theta}{dt^2} + \omega^2 \theta = \frac{R}{I} F(t) \quad (6)$$

where

$$\omega^2 = \frac{1}{I} \left[\int_0^R gr dm_p + m_s g R \right] \quad (7)$$

Anderson and Knight have developed an analytical model to predict $F(t)$ for inviscid and perfect gas.¹⁶ The force from the cavity is given by Eq. (8) assuming that the flow is initially sonic at the throat (see Anderson and Knight¹⁶).

$$\frac{F(t)}{p_\infty A} = \begin{cases} 0 & \text{for } t < t_o \\ c(\gamma) \left[1 + (\gamma - 1) \frac{Q\eta}{p_\infty V} \right] [1 + \beta(t - t_o)]^{-\frac{2\gamma}{\gamma-1}} - 1 & \text{for } t_o \leq t \leq t_o + t_1 \\ \left(\frac{2\gamma}{\gamma-1} \right) \left[\left(\frac{p_t}{p_\infty} \right)^{\frac{\gamma-1}{\gamma}} - 1 \right] & \text{for } t > t_o + t_1 \end{cases} \quad (8)$$

where Q is the energy deposited into the cavity, V is the cavity volume, p_∞ is the ambient pressure, A is the cavity exit area, and η is the thermal efficiency. The energy deposition is assumed to occur instantaneously. The constants are given by the following relations

$$c(\gamma) = \left(\frac{2\gamma}{\gamma+1} \right)^{\frac{1}{\gamma-1}} \quad (9)$$

$$G = \left(\frac{2}{\gamma - 1} \right) \left(\frac{\gamma + 1}{2} \right)^{\frac{\gamma+1}{2(\gamma-1)}} \quad (10)$$

$$\beta = \frac{a_{to}A}{GV} \quad (11)$$

where a_{to} is the initial speed of sound in the cavity

$$a_{to} = \sqrt{\gamma R T_{to}} \quad (12)$$

and the initial temperature in the cavity can be found from Eq. (2)

The condition for initially sonic flow at the cavity exit (see Anderson and Knight¹⁶) is

$$\epsilon = \frac{Q\eta}{p_\infty V} > \frac{1}{\gamma-1} \left[\left(\frac{\gamma+1}{2} \right)^{\gamma/(\gamma-1)} - 1 \right] \simeq 2.23 \text{ for } \gamma = 1.4 \quad (13)$$

The time interval t_1 of sonic flow at the cavity exit is

$$t_1 = 8.64 \left(\frac{V}{a_{to}A} \right) \left[0.9129 \left(1 + 0.4 \frac{\eta Q}{p_\infty V} \right)^{1/7} - 1 \right] \quad \text{for } \gamma = 1.4 \quad (14)$$

The total pressure ratio to ambient pressure during subsonic flow at the cavity exit is determined by the following implicit equation¹⁶

$$\mu \sqrt{\mu^2 + 1} (2\mu^2 + 5) + 3 \log(\mu + \sqrt{\mu^2 + 1}) - 3.946 + \left(\frac{8}{\sqrt{5}} \right) \left(\frac{a_{to}A}{V} \right) \frac{t - (t_1 + t_o)}{(1 + 0.4\epsilon)^{1/7}} = 0 \quad \text{for } \gamma = 1.4 \quad (15)$$

where

$$\mu = \sqrt{\left(\frac{p_t}{p_\infty} \right)^{(\gamma-1)/\gamma} - 1} \quad (16)$$

For initially subsonic throat, $\epsilon < 2.23$, (see Anderson and Knight¹⁶)

$$\frac{F(t)}{p_\infty A} = \left(\frac{2\gamma}{\gamma-1} \right) \left[\left(\frac{p_t}{p_\infty} \right)^{\frac{\gamma-1}{\gamma}} - 1 \right] \quad (17)$$

The total pressure ratio to ambient pressure for subsonic throat is found by the following implicit relation

$$\mu \sqrt{\mu^2 + 1} (2\mu^2 + 5) + 3 \log(\mu + \sqrt{\mu^2 + 1}) - \mu_0 \sqrt{\mu_0^2 + 1} (2\mu_0^2 + 5) - 3 \log(\mu_0 + \sqrt{\mu_0^2 + 1}) + \frac{8}{\sqrt{5}} \frac{(\frac{a_{to}A}{V})(t - t_o)}{\sqrt{\mu_0^2 + 1}} = 0 \quad (18)$$

where μ is found by Eq. (16) and

$$\mu_0 = \sqrt{\left(\frac{p_{t_o}}{p_\infty} \right)^{(\gamma-1)/\gamma} - 1} \quad (19)$$

where

$$\frac{p_{t_o}}{p_\infty} = 1 + (\gamma - 1)\epsilon \quad (20)$$

The total discharge time for initially sonic throat, $\epsilon > 2.23$, is

$$t_f = \frac{V}{a_{to}A} \left[8.99(1 + 0.4\epsilon)^{1/7} - 8.64 \right] \quad (21)$$

and the total discharge time for initially subsonic throat, $\epsilon < 2.23$, is

$$t_f = \left(\frac{V}{a_{t_0} A} \right) \frac{\sqrt{5}}{8} \left(\frac{p_{t0}}{p_\infty} \right)^{1/7} \left\{ \sqrt{\left(\frac{p_{t0}}{p_\infty} \right)^{2/7} - 1} \left[2 \left(\frac{p_{t0}}{p_\infty} \right)^{3/7} + 3 \left(\frac{p_{t0}}{p_\infty} \right)^{1/7} \right] + 3 \log \left[\left(\frac{p_{t0}}{p_\infty} \right)^{1/7} + \sqrt{\left(\frac{p_{t0}}{p_\infty} \right)^{2/7} - 1} \right] \right\} \quad (22)$$

where ϵ and $\frac{p_{t0}}{p_\infty}$ are given by Eq. (2) and (20), respectively.

III.C. Numerical Method

The governing equation (Eq. (6)) is second order in time and therefore requires two initial conditions, the specification of θ and $d\theta/dt$ at the initial time (see Anderson and Knight¹⁷). The angle θ and the angular velocity $d\theta/dt$ at the instant of spark discharge are obtained from the experiment by matching the time of spark discharge and pre-spark amplitude of the pendulum oscillation. The natural frequency, ω , is obtained from the experiment subsequent to the discharge.

For all the cases there is a displacement offset which is the mean of the experimental data. For all cases the offset is subtracted from the displacement data before and after the pulse to examine the effect of discharge and exclude other effects on oscillations. The energy efficiency η is determined by choosing the value that creates a match between theoretical displacement and experimental displacement.

To solve the second-order differential equation (Eq. (6)) a fourth order Runge-Kutta scheme¹⁸ is applied with variable time steps for different phases of pre-discharge, discharge (sonic and subsonic throat intervals), and post-discharge. Newton's method is used to find the numerical roots of the implicit relations (Eq. (15) and (18)) to determine $F(t)$.

IV. Results

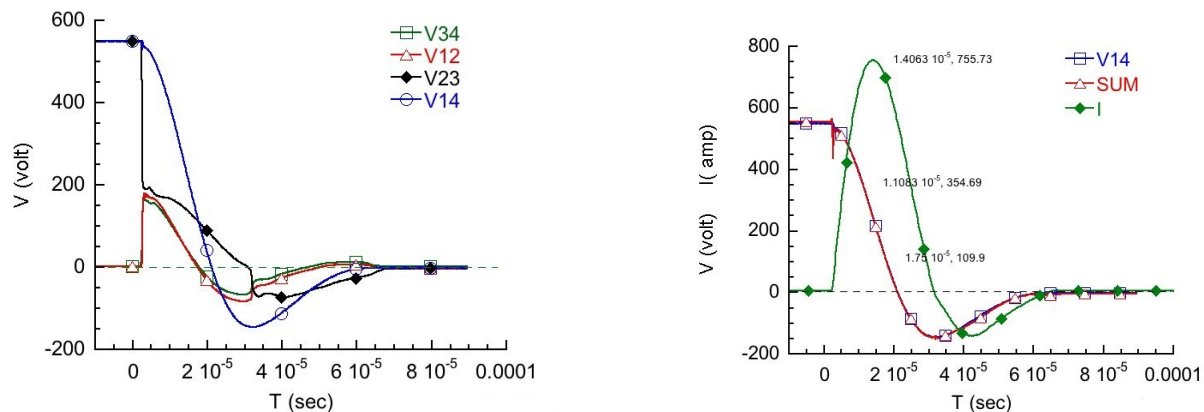
IV.A. Experiment

Fig. 8(a) shows an example of individual voltage drops around the discharge loop in Fig. 4 for the case of $C = 20\mu\text{F}$ where V_{14} denotes the voltage across the capacitor between nodes 1 and 4 with the other voltages following similar notation, *i.e.*, the spark gap voltage drop is V_{23} and the supply and return wires V_{12} and V_{34} , respectively. The low level trigger input occurs at $t = 0$ causing the trigger voltage V_{53} (not shown) to rise until gap 5–3 ionization voltage is reached several microseconds later. At that time, complete ionization of gaps 5–3 and 5–2 occurs (see Fig. 5(a)) and the capacitor begins to discharge. Gap voltage V_{23} abruptly falls to about 200 volt corresponding to the ionization channel resistance at that moment. Simultaneously, the supply and return wires develop voltage drops V_{12} and V_{34} based on their small but finite resistance and the high current magnitude. The three voltages continue to fall as the capacitor discharges as shown by V_{14} . At about 30 microseconds, the falling gap voltage can no longer support the ionization channel and an abrupt change in voltage occurs as the real current flow stops. At that point, the energy deposition ceases. The large undershoot in voltage V_{14} is due to resonance effects in the series RLC circuit formed by loop 1–2–3–4. The sudden current flow beginning several microseconds after $t = 0$ creates a magnetic field around the discharge loop wires. As that field collapses, it induces a back emf opposite in sign to the initial voltage. If the back emf excursion is large enough, it can create a second spark discharge. The back emf can be blocked with a diode to avoid that situation (see Fig. 4).

Fig. 8(b) shows the sum of gap and wire voltage drops compared to the source capacitor voltage. The diode in Fig. 4 was reused in this measurement in order to show the complete wave forms. According to Kirchhoff's voltage law, the sum of the voltages around a loop must equate to zero, or equivalently in this case, $V_{14} = V_{12} + V_{23} + V_{34}$. Other than evidence of the trigger pulse near $t = 0$, there is virtually no difference between the capacitor voltage, V_{14} , and the sum of the loop voltages, V_{12} , V_{23} , and V_{34} . This is a highly significant finding since it demonstrates that 100% of the supplied energy by the capacitor is accounted for by considering only the spark gap and the connecting wires. That means that no significant leakage currents exist including through the connected trigger circuit or as radiated energy. The measured energy dissipated in the spark gap is the proper value to use in computing SparkJet efficiency and not the total capacitor electrical energy, $E = \frac{1}{2}CV^2$.

Also shown in Fig. 8(b) is the instantaneous current waveform. Note that the peak current occurs at the maximum slope, dV/dt , of the capacitor discharge voltage as expected. The value of the capacitance computed from the rate of change of voltage and the measured current, $C = \frac{I}{dV/dt}$, varies by only 10% from

the capacitor's label value at the peak in the current waveform. The label value is $20\mu\text{F}$ and the computed value at the current peak is $22.3\mu\text{F}$.



(a) Individual element voltage drops around discharge loop consisting of capacitor, connecting wires and spark gap. Notation corresponds to nodes in Fig. 4. Symbols are for curve identification. $C = 20\mu\text{F}$

(b) Capacitor voltage compared to sum of discharge loop voltage drops from Fig. 8(a)

Figure 8. Voltage Drops

Fig. 9 shows typical spark gap voltage, current and power waveforms for the case of $C = 20\mu\text{F}$. In this case, a diode was used to block the field-induced back emf to permit just a single positive current pulse. The power curve is the product of the voltage and current. The integral of the power with respect to time over the pulse duration is equal to the total energy deposited into the spark. In this case, the energy input is just over 1 joule. Compare this to the electrical energy stored by the capacitor, $E = 0.5 \times (20 \times 10^{-6}) \times 5502 = 3.02$ joule and it is seen that *two-thirds* of the capacitor total energy is lost to the wiring resistance.

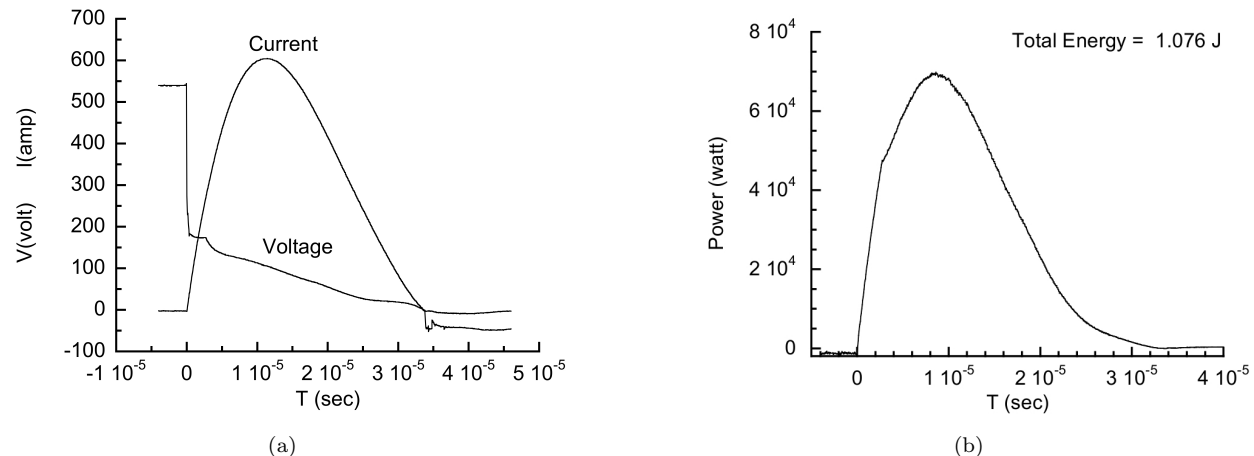
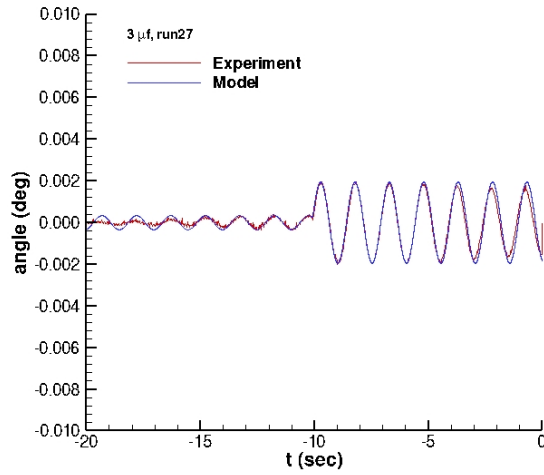


Figure 9. Typical spark gap voltage, current and power waveforms, $C = 20\mu\text{F}$

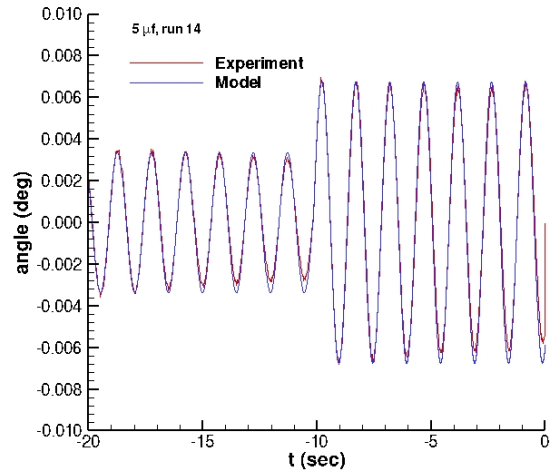
This was the procedure used to compute Q for the range of capacitances tested in this experiment. Also note that the pulse width (about 25 microseconds) is nearly five orders of magnitude less than the period of the pendulum, 1.5 sec, showing that the energy deposition can be reasonably modeled as instantaneous.

IV.B. Theory

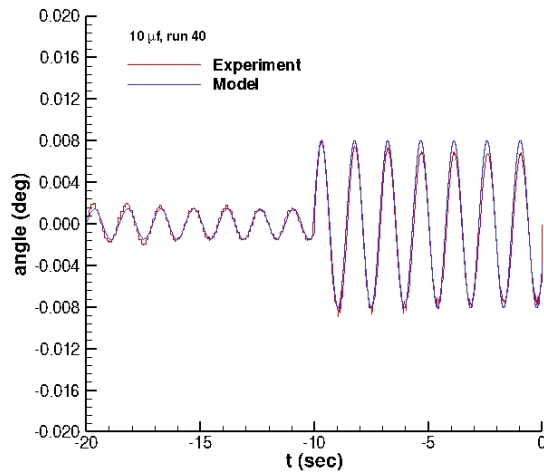
Theoretical results are shown in Fig. 10 for a single run each from various experiments with $C = 3, 5, 10, 20$, and $40 \mu\text{F}$. It should be noted that the computed efficiency likely depends upon the details of this particular SparkJet design. Moreover, further research is in progress to determine the sensitivity of the computed efficiency to the energy of the capacitive discharge.



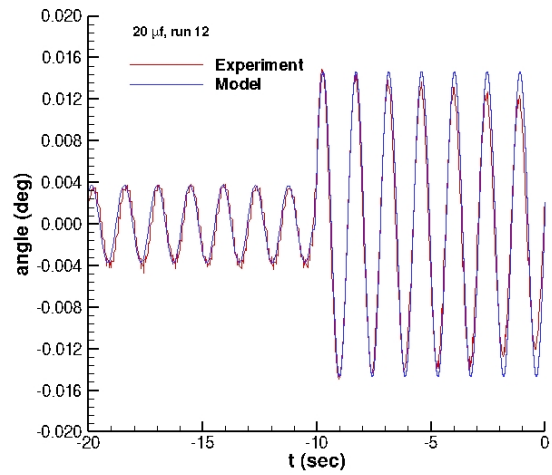
(a) $\eta = 8.91\%$ and $Q = 181$ mJ



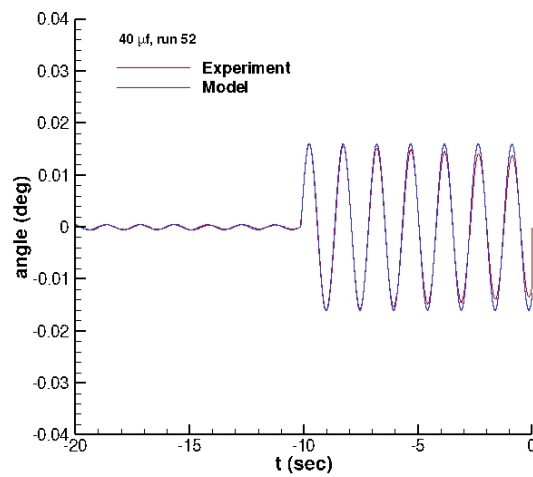
(b) $\eta = 8.56\%$ and $Q = 285$ mJ



(c) $\eta = 6.67\%$ and $Q = 572$ mJ



(d) $\eta = 4.72\%$ and $Q = 1130$ mJ



(e) $\eta = 3.97\%$ and $Q = 1901$ mJ

Figure 10. Experiment *vs* theory
10 of 12

The average efficiency and standard deviation values of multiple runs (5 to 10) for different capacitances are summarized in Fig. 11(a). The average efficiency and standard deviation values for different values of dimensionless deposited energy are plotted in Fig. 11(b). The result indicates lower efficiencies with higher capacitances which correspond to discharges resulting in initially sonic throat in the cavity.

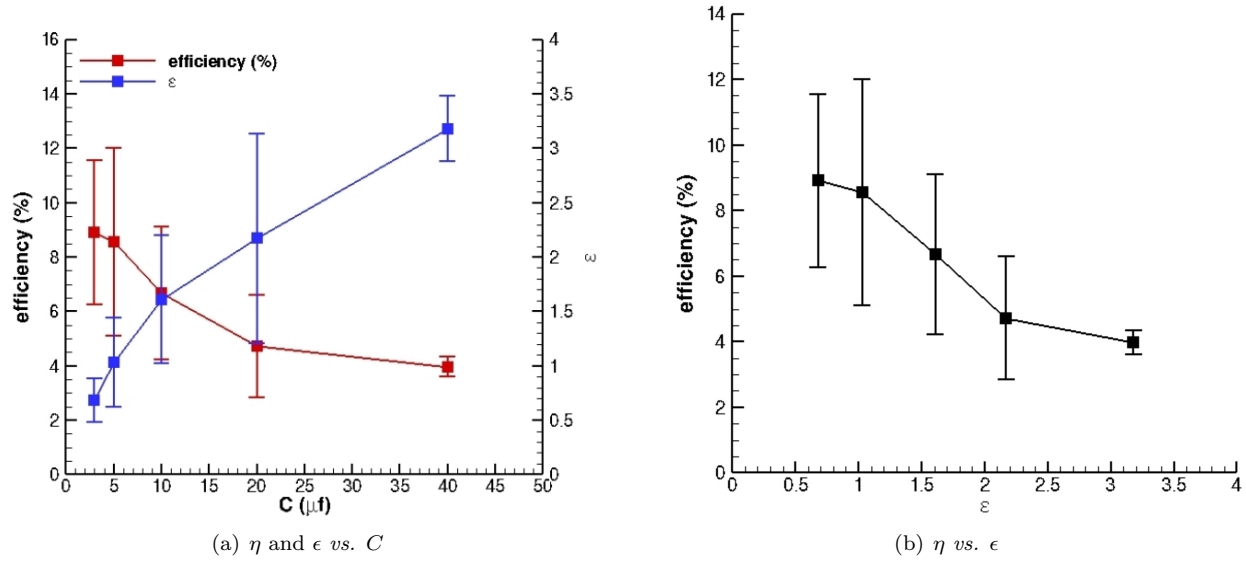


Figure 11. Thermal efficiency and dimensionless energy deposition parameter

V. Conclusion

A novel method for determining the thermal efficiency of the SparkJet is proposed. The thermal efficiency is the fraction of the capacitive discharge energy which is channeled into heating of the gas (*i.e.*, increasing the translational-rotational temperature). A SparkJet is attached to the end of a free swinging pendulum. The displacement of the pendulum *vs* time due to a single SparkJet discharge is measured using a laser displacement sensor. A theoretical model for the SparkJet thermal efficiency is developed assuming a perfect gas. The thermal efficiency of the SparkJet is calculated by fitting the predicted displacement *vs* time with the experiment. The results indicate less than 10% efficiency depending on the capacitance size. In addition, the efficiency decreases with larger energy deposition magnitudes.

Acknowledgments

The theoretical portion of this research is supported by the US Air Force Office of Scientific Research under Grant FA9550-10-1-0111, managed by Dr. John Schmisser, and the experimental portion by NASA Langley Research Center.

References

- ¹Fomin, V., Tretyakov, P., and Taran, J.-P., "Flow Control Using Various Plasma and Aerodynamic Approaches (Short Review)," *Aerospace Science and Technology*, Vol. 8, 2004, pp. 411–421.
- ²Bletzinger, P., Ganguly, B., Van Wie, D., and Garscadden, A., "Plasmas in High Speed Aerodynamics," *Journal of Physics D: Applied Physics*, Vol. 38, 2005, pp. R33–R57.
- ³Corke, T., Post, M., and Orlov, D., "Single-Dielectric Barrier Discharge Plasma Enhanced Aerodynamics: Concepts, Optimization, and Applications," *Journal of Propulsion and Power*, Vol. 24, No. 5, 2008, pp. 935–945.
- ⁴Shin, J. and Mahadevan, S., "Forcing Mechanisms in Supersonic Flow Actuation by Direct Current Surface Glow Discharge Plasma," *Aerospace Science and Technology*, Vol. 15, 2011, pp. 18–24.
- ⁵Grossman, K., Cybyk, B., Rigling, M., and Van Wie, D., "SparkJet Actuators for Flow Control," AIAA Paper 2003-0057, American Institute of Aeronautics and Astronautics, Reston, VA, January 2003.
- ⁶Cybyk, B., Grossman, K., Wilkerson, J., Chen, J., and Katz, J., "Single-Pulse Performance of the SparkJet Flow Control Actuator," AIAA Paper 2005-0401, American Institute of Aeronautics and Astronautics, Reston, VA, January 2005.

- ⁷Cybyk, B., Simon, D., Land, H., Chen, J., and Katz, J., “Experimental Characterization of a Supersonic Flow Control Actuator,” AIAA Paper 2006-0478, American Institute of Aeronautics and Astronautics, Reno, NV, January 2006.
- ⁸Cybyk, B., Wilkerson, J., and Simon, D., “Enabling High-Fidelity Modeling of a High-Speed Flow Control Actuator Array,” AIAA Paper 2006-8034, American Institute of Aeronautics and Astronautics, Reston, VA, January 2006.
- ⁹Haack, S., Land, B., Cybyk, B., Ko, H., and Katz, J., “Characterization of a High-Speed Flow Control Actuator Using Digital Speckle Tomography and PIV,” AIAA Paper 2008-3759, American Institute of Aeronautics and Astronautics, Reston, VA, June 2008.
- ¹⁰Haack, S., Taylor, T., Emhoff, J., and Cybyk, B., “Development of an Analytical SparkJet Model,” AIAA Paper 2010-4979, American Institute of Aeronautics and Astronautics, Reston, VA, June 2010.
- ¹¹Haack, S., Taylor, T., Cybyk, B., Foster, C., and Alvi, F., “Experimental Estimation of SparkJet Efficiency,” AIAA Paper 2011-3997, American Institute of Aeronautics and Astronautics, Reston, VA, June 2011.
- ¹²Narayanswamy, V., Shin, J., Clemens, N., and Raja, L., “Investigation of Plasma-Generated Jets for Supersonic Flow Control,” AIAA Paper 2008-0285, American Institute of Aeronautics and Astronautics, Reston, VA, January 2008.
- ¹³Caruana, D., Barricau, P., Hardy, P., Cambronne, J., and Belinger, A., “The ‘Plasma Synthetic Jet’ Actuator - Aerothermodynamic Characterization and First Flow Control Applications,” AIAA Paper 2009-1307, American Institute of Aeronautics and Astronautics, Reston, VA, January 2009.
- ¹⁴Anderson, K. and Knight, D., “Characterization of Single Pulse of Plasma Jet,” AIAA Paper 2012-0188, American Institute of Aeronautics and Astronautics, January 2012.
- ¹⁵Reedy, T., Kale, N., Dutton, J. C., and Elliott, G., “Experimental Characterization of a Pulsed Plasma Jet,” AIAA Paper 2012-0904, American Institute of Aeronautics and Astronautics, January 2012.
- ¹⁶Anderson, K. and Knight, D., “Plasma Jet for Flight Control,” *AIAA J.*, Vol. 50, 2012, pp. 1855–1872.
- ¹⁷Anderson, K. and Knight, D., “Energy Deposition Induced Synthetic Jet for Flow Control,” CCD Report 2011-3, Rutgers University, 2011.
- ¹⁸Burden, R. and Faires, J., *Numerical Analysis*, Brooks/Cole Publishing Company, Pacific Grove, CA, 1997.